Analytical and numerical simulations of an Oscillating Water Column with humidity in the air chamber

Analytical and numerical simulations of an Oscillating Water Column with humidity in the air chamber

E. Medina-López[a,b], A.G.L. Borthwick[a], A. Moñino[b]

[a] *Institute for Infrastructure and Environment. School of Engineering. University of Edinburgh. The King's Buildings, EH9 3JL Edinburgh (United Kingdom)*

[b] *Andalusian Institute for Earth System Research, Universidad de Granada. Av. del Mediterráneo s/n. 18006, Granada (Spain)*

Abstract

This paper examines an Oscillating Water Column (OWC) model, where the air chamber is represented as a dry air–water vapour mixture, based on the thermodynamics of a real gas. The novelty of this study consists of the inclusion of humidity effects on the general performance of the OWC and its coupling with the radiation–diffraction problem of the device. Using FLUENT®, a numerical 2D flume is built to simulate wave–induced flow in the OWC. Air phase properties are adjusted to represent the presence of moisture. Turbine linear performance, according to a standard Wells turbine power take–off system, is simulated by means of an Actuator Disk Model (ADM). Numerical outputs are compared with analytical solutions of the classic OWC radiation–diffraction problem, in which the theoretical real gas model is embedded. Results show that the use of real gas thermodynamic theory reduces considerably the predicted power output of OWC devices, with theoretical losses reaching 50% in certain cases. The effect of humidity mitigates resonant conditions. Techno–economic considerations justify the inclusion of real gas theory to achieve competitive devices.

Keywords: Oscillating Water Column (OWC), Actuator Disk Model (ADM), real gas, FLUENT®, humidity, radiation–diffraction

1. Introduction

As one of the leading candidate technologies for wave energy conversion, the oscillating water column (OWC) has received substantial attention over recent decades, Cruz (2008), Falcão (2010). At the time of writing, OWC–based power plants have already been installed at many locations around the world, *e.g.* in Portugal, Scotland, Spain, India, Australia and China. The OWC consists of a partially submerged chamber, with a gap at the bottom allowing transmission of the oscillation induced by impinging waves on the device, and is equipped with a power take–off system (PTO) for energy transformation, usually comprising a Wells turbine Gato & Falcão (1984), Raghunathan

Email address: emedina@ed.ac.uk (E. Medina-López)

(1995). Wells turbines exhibit linearity between flow discharge and pressure drop and reversibility in terms of flow direction, *i.e.* the rotation direction is always the same, thus improving performance in an oscillating flow. The water column oscillation induces time–dependent compressions and expansions of the gas phase inside the chamber, and conversion of pneumatic energy into electricity to be supplied to the grid.

Although the available power resource from ocean waves appears to be huge, there are many key technical, financial, political and social acceptance issues to be solved. For example, there is a considerable gap between conceptual design and economically feasible technical implementation, SI Ocean (2014–I,-,-). Major investment, policy and social challenges need to be overcome, including social acceptance, exemplified by the NIMBY (Not In My BackYard) attitude, and potential environmental consequences, Heras–Saizarbitoria *et al.* (2013), Hitzeroth & Megerle (2013). In Europe, where more than 60% of the WECs designed are oriented to offshore deployment, difficulties in servicing and repair, connection to the grid, and survivability are problems yet to be addressed Magagna & Uihlein (2015).

To date, formulations of OWC physics have usually been developed in terms of radiation–diffraction problems. Analytical solutions devised using linear theory, Evans (1982), Sarmento & Falcão (1985), Evans & Porter (1995), provide relatively accurate descriptions of wave–device interaction, oscillation of the water column inside the OWC, and hence global efficiency of the device. Attention has focused on several aspects of OWC devices related to influence of boundary conditions, Martins–Rivas & Mei (2009–I,-), Lovas *et al.* (2010), control of PTO turbine performance, improvements in OWC plant management, Gato & Falcão (1989), Justino and Falcão (1999), Falcão & Justino (1999), Falcão *et al.* (2016), mutual interaction between turbine damping and wave and tidal conditions, López *et al.* (2014, 2015), performance optimization in terms of geometry, Zhang *et al.* (2012), and influence of seabed slope and bed evolution on global performance and efficiency of OWCs, Rezanejad *et al.* (2013(@, 2015), Medina-Lopez *et al.* (2017–II, 2018). Tools have been developed for integrated modelling of the OWC, Mendoza *et al.* (2017), and optimized design carried out in terms of wave–forcing time scales, Jalón *et al.* (2016). Numerical and experimental research has led to further advances concerning OWC performance and efficiency, by examining specific features that are otherwise hard to observe in full–scale prototypes. Researchers have studied the coupling between aerodynamic and hydrodynamic features through numerical simulation, Teixeira *et al.* (2013), OWC efficiency according to non linear analysis, Luo *et al.* (2014), and implementation of PTO turbine linear performance through Actuator Disk Model theory, Moñino *et al.* (2017). Research studies have also considered verification of OWC models, Iturrioz *et al.* (2015), turbine damping control, Rezanejad *et al.* (2017), and specific chamber set up configurations, Bingham *et al.* (2015), Elhanafi *et al.* (2017).

A key factor in the study of an OWC is the thermodynamics of the gas phase inside the chamber. It is usually assumed that the gas phase comprises dry air, which is treated as ideal gas undergoing adiabatic polytropic processes of compression and expansion. The air process inside the chamber has been the subject of several studies Falcão & Justino (1999), Zhang *et al.* (2012), Sheng *et al.* (2013), none of which considered the effect of assumptions of gas phase and thermal isolation of the processes. While it is reasonable

to assume the adiabatic nature of the air cycle inside the chamber, consideration of gas phase constituents, *i.e.* a mixture of dry air and water vapour, should lead to a more realistic representation of the thermodynamics inside the OWC chamber, and hence actual working conditions in a full scale prototype. Deviations from ideal gas performance have been experimentally observed in a stationary two–phase air–water vapour flow through an OWC chamber model, Medina-Lopez *et al.* (2016). Moreover, implementation of a real gas formulation in the OWC thermodynamics, based on the virial Kammerlingh–Onnes expansion, Prausnitz (1999), Wisniak (2003), Tsonopoulos & Heidman (1990), leads to a lower estimate of global efficiency of the OWC, which might provide an explanation for differences between predicted global efficiency and previously reported values, Medina-Lopez *et al.* (2017–I).

All the previous findings contribute to the development of wave energy extraction technology, related to the main barriers involved in ocean energy development: technology advancement, environment, investment and social acceptance. Considering the European scenario as an example, the target is that by 2020 the energy farmed from clean sources should supply 20 % of the total energy demand, O'Hagan *et al.* (2016). Indeed, future prospects indicate that up to 26 MW could be available from wave energy by 2020, Magagna & Uihlein (2015). With a perspective of more than 60 % of the wave energy future projects pointing to off–shore extraction (locations around 10 km away from the coast), efforts are required to make the wave energy technology a trustworthy option. If we think in terms of off–shore wind energy, for example, considerable advances have already been achieved, taking advantage of on–shore experience, and a roughly 1 : 5 ratio between installed MW and million Euro invested has been reached. However, in the case of off–shore wave energy, that ratio is drastically altered towards investment, reaching a ratio of 1 : 10, see NOEP (2017).

It is necessary to bridge certain technical gaps to build easy–to–deploy prototypes with cost–effective installation, and more importantly, with cost–effective maintenance and replacement features. Focusing now on the case of OWC technology, a deeper knowledge is required of the factors affecting the PTO efficiency. Known limitations on turbine performance such as thermodynamic conditions due to air state, are essential to fix these issues and to direct properly the research efforts. For example, rather than a high–cost device with a longer service life and able to work under high energy wave climate, *i.e.* more than 50 kW/m, it would be more effective to develop low–cost devices with known efficiency limitations, but able to operate almost permanently under mild climate conditions and with easy–to–replace components, in which the main investment part would concern the foundation and connection to the grid. These facts are addressed in this paper, starting by studying the actual conditions of OWC devices in thermodynamic terms, and linking these with wave–structure interaction. The methodology presented in this paper is a step to a more accurate estimation of efficiency and working conditions, leading to a reduction in risk and uncertainty, and thus increasing the OWCs reliability.

From the previous scope, this paper examines the gas phase cycle of a simplified OWC, incorporating real gas thermodynamics. The theory is implemented in the classical radiation–diffraction problem, following Medina-Lopez *et al.* (2017–I). A complete numerical 2D domain in FLUENT® is used to verify the theoretical approach and

investigate its reliability. Wells turbine linear performance is modelled using an actuator disk model, Moñino *et al.* (2017). The results are found to be consistent with theoretical predictions, contributing to a better understanding of OWC performance and thermodynamics governing its efficiency. A discussion on the effects of this theory on OWC design and cost is included as a conclusion to this paper.

2. Methodology

Following Medina-Lopez *et al.* (2017–I), real gas thermodynamics is implemented in the classical formulation of the radiation–diffraction problem, in order for the gas phase inside the OWC, a mixture of dry air and water vapour, to undergo an adiabatic compression and expansion cycle. Here, the polytropic equation is corrected to account for real gas. Different thermodynamic conditions in terms of water vapour concentration are considered, *i.e.* from dry air to 100 % saturated dry air–water vapour mixture. Please note that equations (1) to (4) have been published in Medina-Lopez *et al.* (2017–I).

To study the performance of the OWC wave energy converter, a rectangular chamber is inserted so that it is partially submerged under the free surface of water in a computational wave tank. The PTO comprising the Wells turbine is represented by an actuator disk model, which is validated with experimental data. The OWC design is taken from Moñino *et al.* (2017), which utilises an actuator disk model to simulate a Wells turbine.

Table 1 lists the acronyms used for the models considered herein, including that by Medina-Lopez *et al.* (2017–I) (AM2). The classical formulation of OWC behaviour is represented by AM1. Humidity is introduced in the gaseous phase (NM2) of the numerical model presented by Moñino *et al.* (2017) (NM1), and a comparison is carried out between the theoretical real gas model for OWC (AM2) and numerical results (NM1 and NM2). The initial formulation proposed by Medina-Lopez *et al.* (2016) is used to solve numerically the equations presented in the present paper.

	Dry air	Humid air
Analytical	AM1	AM2
Numerical	NM1	NM2

Table 1: Models and their acronyms.

3. Real gas analytical model for OWC formulation

A summary of the formulation derived by Medina-Lopez *et al.* (2017–II) is first presented. The general expression of the adiabatic coefficient for a real gas is:

$$n = \frac{C_p/C_v}{1 - \dfrac{p}{\mathbb{Z}}\left(\dfrac{\partial \mathbb{Z}}{\partial p}\right)_T} \tag{1}$$

where C_p is specific heat at constant pressure, C_v is specific heat at constant volume, p is pressure, $\mathbb{Z}$ is compressibility factor, and T is temperature. After rearranging, equation (1) simplifies to give:

$$n = \mathbb{Z}\frac{C_p}{C_v} \tag{2}$$

Considering the inhalation and exhalation processes separately within the OWC air chamber, the flow of real gas through the turbine is expressed by:

- Inhalation

$$Q_T = \left(1 + \frac{p_g}{np_0}\right) Q_{owc} - \frac{V}{np_0}\frac{dp_g}{dt} - \frac{Vp_g}{p_0}\frac{d(1/n)}{dt} \tag{3}$$

- Exhalation

$$Q_T = Q_{owc} - \frac{V}{n(p_0 + p_g)}\frac{dp}{dt} - \frac{Vp_g}{p_0 + p_g}\frac{d(1/n)}{dt} \tag{4}$$

where p_g is pressure inside the OWC considering the real gas formulation, p_0 is the reference pressure, Q_{owc} is the water flow due to water column displacement, V is volume, and t is time. These expressions are equivalent to those presented by Sheng *et al.* (2013), but with the addition of real gas terms.

3.1. Coupling with radiation–diffraction theory

Equations (3) and (4) are now inserted in the classic OWC formulation, given by Martins–Rivas & Mei (2009–I). The goal is to obtain a new expression for power including the properties of real gas, and hence develop a global model that takes into account thermodynamic and mechanical effects inside the OWC chamber. The real gas model is expected to modify the radiation–diffraction problem because the energy of humid air inside the chamber is different to that of dry air. Here, wave–structure interaction in OWC is treated as separate radiation and diffraction problems. The radiation problem is defined by Martins–Rivas & Mei (2009–I) as the effect of the pulse of pressure produced inside the OWC chamber on the water surface elevation, assuming that the top of the device is closed. The diffraction problem is defined as the interaction between waves and structure, assuming there is no restriction on the air moving up through the device to the open top (in other words, the turbine effect is not considered in the diffraction problem).

For the coupled real gas wave–structure interaction model, the revised gas properties are expected to produce a different damping effect inside the chamber, modifying radiation. The effect on the diffraction part is not so obvious, given that air properties

are constant inside and outside the chamber. Noting that the diffraction and radiation problems are linked, a coupled approach is developed below.

To evaluate the power for real gas, the pressure equation is modified, utilising airflow expressions obtained by Medina-Lopez *et al.* (2017–I). These expressions are linked to the turbine characteristic equation, presented by Martins–Rivas & Mei (2009–I), in order to link the airflow inside the OWC chamber (Q_T) and the water flow due to the water column displacement ($Q_{owc} = dV/dt$):

$$\frac{dm}{dt} = \rho_g \frac{dV}{dt} + V\frac{d\rho_g}{dt} = \frac{KD}{N} p_g \,, \tag{5}$$

where K is a coefficient depending on turbine geometry, D is turbine diameter, and N is rotational speed in revolutions per minute of the turbine. In this case, the same variables considered by Martins–Rivas & Mei (2009–I) have been used, namely: $K = 0.45$, and $N = 2000\,\text{r.p.m.}$

The volumetric flow rate of water Q_{owc} is then related to radiation and diffraction coefficients through:

$$Q_{owc} = Q^R + Q^D = -(\mathbb{B} - i\mathbb{C})p_g + \Gamma A_0 \tag{6}$$

where Q^R is the radiated flow rate, Q^D is the diffracted flow rate, $\mathbb{B}$ and $\mathbb{C}$ are the radiation coefficients, and Γ is the diffraction coefficient. A_0 is the incoming wave amplitude. The radiation and diffraction coefficients are obtained through the formulation given by Martins–Rivas & Mei (2009–I) using a program implemented in Python Jalón (2016). This new pressure takes into account the properties of real gas and is a better approximation to the actual working conditions. Power is then calculated following Martins–Rivas & Mei (2009–I) (see Appendix I for the developed expression) from:

$$P = \frac{KD}{N\rho_g}|p_g|^2 \,. \tag{7}$$

3.1.1. Real gas pressure inside the OWC chamber

Expressions for pressure incorporating the effect of real gas for both inhalation and exhalation phases are obtained by substituting (3) and (5) into (6). The complete development is shown in Appendix II, and the values of each coefficient in equations (8) and (9) are specified there. The final equations used in the next sections of the paper are the following:

- Inhalation

$$p_g^{in} = \frac{A_0\, N\, \Gamma\, \rho_0 \,+\, \alpha \,-\, D\, K\, n\, p_0 \,+\, \zeta \,-\, \kappa \,+\, \varepsilon \,+\, \vartheta}{\psi} \tag{8}$$

- Exhalation

$$p_g^{ex} = -\frac{D\, K\, n\, p_0 \,-\, \tau \,+\, \zeta_g \,+\, \varsigma \,-\, \kappa_g \,+\, \varepsilon_g \,-\, \vartheta_g}{\varrho} \tag{9}$$

Application of coupled real gas–radiation–diffraction analytical model to a hypothetical pulse of pressure

In order to compare the differences between real and ideal gas models, the same hypothetical pulse of pressure analysed by Medina-Lopez *et al.* (2017–I) is now applied to the coupled real gas–radiation–diffraction model. The pulse of pressure is used to trigger the system formed by n and p_g^{in} (see equations (2) and (8), respectively).

Table 2 summarises the simulated wave conditions considered and their related non–dimensional radiation coefficients ($\tilde{\mathbb{B}}$ and $\tilde{\mathbb{C}}$). Here the diffraction coefficient is calculated from (Evans & Porter (1995)),

$$\tilde{\Gamma} = \left| \sqrt{\frac{4\tilde{\mathbb{B}} C_g \omega}{kag}} \right| , \tag{10}$$

where C_g is wave group celerity, ω is wave frequency, k is wave number, a is the OWC radius, and g is gravitational acceleration. It should be noted that results for the real gas model were found to have a very weak dependence on the value of the diffraction coefficient Γ. By definition, the diffraction–radiation problem implies that phenomena inside the OWC chamber solely cause variations in the radiation coefficients.

The wave height H is taken as a fixed parameter, noting that the numerical tests showed that the wave period, T, was the dominant parameter, with the choice of value for H having negligible effect on results. Submergence of the OWC device is fixed at 2 m, and the water depth is $h = 10$ m. Three different OWC diameters are used to compare geometry scale effects: $D = 20\,, 10\,, 5$ m (corresponding to $a/h = 1$, $a/h = 0.5$, and $a/h = 0.25$). The results were obtained using a numerical solver developed by Jalón (2016). a is the OWC radius.

		$a/h = 1$		$a/h = 0.5$		$a/h = 0.25$	
$T(s)$	kh	$\tilde{\mathbb{B}}$	$\tilde{\mathbb{C}}$	$\tilde{\mathbb{B}}$	$\tilde{\mathbb{C}}$	$\tilde{\mathbb{B}}$	$\tilde{\mathbb{C}}$
12.56	0.5275	0.1796	0.9825	0.0235	0.4515	0.0029	0.2154
6	1.2980	3.6088	4.0993	0.6026	2.3516	0.0809	1.0548
4	2.5462	12.5630	2.0513	5.3191	5.7734	1.2891	3.8108
3	4.4726	0.6272	0.1511	16.6568	3.2331	6.3360	7.4048
2.5	6.4389	6.9515	12.9499	6.9136	12.3221	15.7919	7.9301

Table 2: Radiation coefficients for $a/h = 1$, $a/h = 0.5$ and $a/h = 0.25$.

The non–dimensional radiation and diffraction coefficients are related to their dimensional counterparts by the following equations Martins–Rivas & Mei (2009–I):

$$(\tilde{\mathbb{B}}, \tilde{\mathbb{C}}) = \frac{(\mathbb{B}, \mathbb{C})}{\left(\dfrac{a}{\omega \rho_w}\right)} , \tag{11}$$

and

$$\tilde{\Gamma} = \frac{\Gamma}{\left(\frac{ag}{\omega}\right)}\,, \tag{12}$$

where a is the OWC radius, ω is the wave frequency, and ρ_w is the water density. A brief outline of the formulation presented by Martins–Rivas & Mei (2009–I) is given in Appendix I.

Fig. 1 shows the ratio between real gas power output (P_r) obtained from equation (7) for the real value of pressure calculated from (8), and ideal gas power output (P_i) as presented by Martins–Rivas & Mei (2009–I).

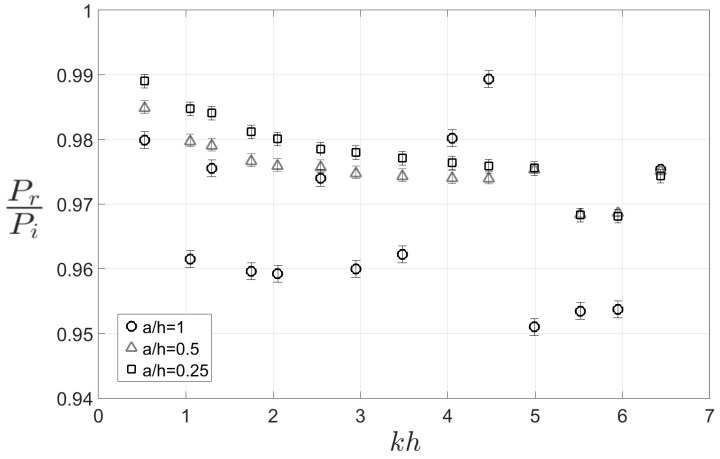

Figure 1: Power ratio for real and ideal gas approaches as a function of depth parameter kh.

Fig. 1 shows that at lower values of kh (equivalent to larger wave periods), the real and ideal gas estimates of power are almost the same. As the wave number increases, there is a noticeable decrease in power ratio, up to a 5% difference between real and ideal gas estimates. For $kh = 4.7$, and $a/h = 1$, a secondary peak occurs, as also observed in the relationship between capture length (kL) and normalised wave number kh obtained by Martins–Rivas & Mei (2009–I).

The capture length of an OWC depends on the radiation and diffraction coefficients, OWC geometry, and wave parameters. However, kL is not independent of the choice between real and ideal gas model. The radiation coefficient depends on the nature of the gas, because the pulse of pressure produced inside the OWC chamber is linked to the process equation. Here, the process equation ($pv^n = constant$) has been modified using the real gas formulation, through changes in the adiabatic coefficient n (see also Medina-Lopez *et al.* (2017–I)). Then, the relationship between volume and pressure accounting for real gas is different to that of the ideal gas formulation. In other words, for a given volume, the pressure inside the chamber when the real gas is taken into

account is different to that of ideal gas. Thus, the radiation effect will be different when the real gas formulation is used.

Despite the difference between real and ideal gas approaches in terms of radiation, resonance remains an important phenomenon in both cases. In Fig. 1, a peak occurs at $kh = 4.7$ for $a/h = 1$, which is not present for the other values of kh considered. This is most likely caused by the relationship between device characteristics and wave conditions, as the resonance frequency is approached.

In short, OWC power outputs in waves of larger periods are less influenced by the choice of real or ideal gas model, and are therefore not considered further. However, for short waves it is recommended that the effect of real gas is taken into account.

4. Numerical model

4.1. Wave generation and OWC simulation in FLUENT®

An OWC structure is appended to a vertical breakwater located at the downstream boundary of the numerical domain. The flume is 120 m long and 12 m high. Still water depth is set to 5 m, Moñino *et al.* (2017). The Wells turbine is represented by means of an Actuator Disk Model (ADM). A piston–paddle is used to generate waves in a dynamic mesh region situated within the overall computational domain. Numerical wave generation is validated by comparing numerical predictions with experimental data, as presented in Moñino *et al.* (2017). Information on the instantaneous paddle position and velocity of the paddle motion is supplied to the upstream boundary of the dynamic mesh region by means of a compiled UDF (User Defined Function) embedded in the solver, according to the *Biésel* theory for a piston–type paddle, as follows, Moñino *et al.* (2017):

$$\begin{aligned} x_{paddle} =& \frac{S_0}{2}\cos\frac{2\pi t}{T}, \\ U_{paddle} =& -\frac{S_0\pi}{T}\sin\frac{2\pi t}{T}, \\ S_0 =& H\frac{2k_0h + \sinh 2k_0h}{4\sinh^2 k_0h}, \end{aligned} \tag{13}$$

where x_{paddle} is horizontal paddle displacement, U_{paddle} is paddle displacement velocity, S_0 is paddle stroke, H is wave height, k is wave number, h is water depth at the paddle location, T is wave period and t is simulation time. The dynamic mesh ensures the harmonic oscillation of the free surface, described by:

$$\begin{aligned} h_{owc} =& h_{ref} - \eta, \\ V_{owc} =& S_{owc}(h_{ref} - h_{owc}), \\ U_{owc} =& \frac{d\eta}{dt} = -\frac{H\pi}{T}\sin\frac{2\pi t}{T}, \end{aligned} \tag{14}$$

where h_{owc} is water surface level inside the OWC, h_{ref} is the reference or initial water level, η is surface elevation, V_{owc} is OWC chamber volume, S_{owc} is horizontal surface of the OWC, and U_{owc} is water displacement velocity within the OWC. The turbine essentially consists of a porous zone that simulates a pressure drop while preserving a continuous distribution of flow velocity. Using ADM theory, a source term is added analytically to the momentum equations. The complete ADM theory development and model set up can be found in Moñino *et al.* (2017).

4.2. FLUENT® solver set up

The numerical domain is meshed in GAMBIT® under a Tri/Pave scheme with maximum spacing setting of 0.1 m and a minimum element size of 0.001 m (the detailed mesh can be observed in Moñino *et al.* (2017)). A pre–meshing scheme is applied to the hub inside the chamber with spacing of 0.01 m, to help achieve a smoother structure in the final mesh. A mesh with 343420 elements is generated. The FLUENT® solver is configured to laminar and VOF (Volume Of Fluid) with air as phase 1 and water as phase 2. The pressure–velocity coupling is set to PISO (Pressure Implicit Split Operator) and the discretionary scheme for pressure is set to PRESTO (Pressure Staggering Options), and first–order upwind is selected for the discretised momentum equation. The free surface reconstruction is set to geo-reconstruct.

Six wave gauges are arranged in the numerical flume, as specified in Fig. 2. Records of total and static pressure, horizontal and vertical velocity, and density distribution, are acquired at 10 Hz sampling rate.

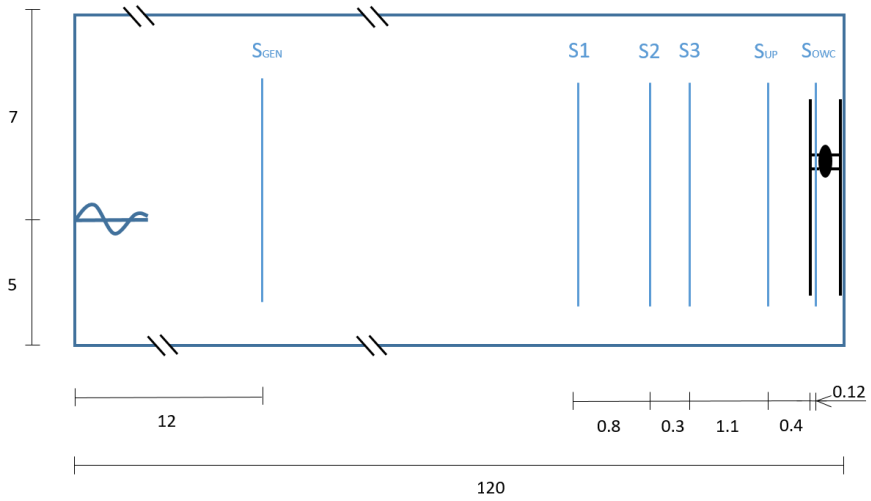

Figure 2: Schematic of gauges located in the numerical flume. Units in m.

The numerical wave generator in FLUENT® was validated against experimental data by Medina-Lopez *et al.* (2017–II). The experiments were carried out in a wave flume

at the *Andalusian Institute for Earth System Research, Universidad de Granada* (Spain).

FLUENT® is able to run simulations with real gases, but only with a density–based solver, Fluent (2006). For the purpose of this paper however, a pressure–based solver is required in order to simulate accurately the interface between water and air. Moreover, if a real gas model were to be used, all fluid zones should contain the real gas or, otherwise, a real gas cannot coexist with another fluid in the same problem. For these reasons, the calculations for real gas inside an OWC cannot be conducted using the real gas tool implemented in the FLUENT® solver. To account for this, humid air is inserted by modification of the standard air conditions given by default. Density, specific heat, and molar weight are specified using the methodology presented by Medina-Lopez *et al.* (2017–I) to fit the characteristics of air according to its humidity. The energy equation is then enabled in the solver in order to take into account the effect of variations in thermal conductivity on the instantaneous specific heat value. The energy equation takes the form:

$$\frac{\partial \rho E}{\partial t} + \frac{\partial}{\partial x_i}(v_i(\rho E + p)) = \frac{\partial}{x_i}\left(k_{eff}\frac{\partial T}{\partial x_i} - \sum_{jn}^{species} h_n J_{ni} + \tau_{ijv_i}\right) + S_h \qquad (15)$$

where E is energy, ρ is fluid density, v_i is the i^{th} velocity component, k_{eff} is effective thermal conductivity obtained as the sum of standard conductivity k and turbulent conductivity k_t, T is temperature, h_j is the n^{th} specie enthalpy, $J_n i$ is the i^{th} diffusion flux component of the n^{th} specie, τ_{ij} is the stress tensor component and S_h represents heat sources included in the problem (such as heat arising from chemical reactions). Equation (15) represents the energy budget when thermal conductivity, species diffusion, and viscosity are accounted for, together with any heat source considered in the problem.

4.3. Insertion of humidity in 2D numerical model containing linear turbine

Humid air is now implemented as the gaseous phase of the numerical model in FLUENT® (model NM2). The combined flume and turbine model used here is the same as described by Moñino *et al.* (2017) (model NM1). Although FLUENT® allows simulations to be run with real gas, such simulations are subject to certain limitations: they can only be run for single phase problems (*e.g.* no multiple fluids involved), and the vapour involved has to be present in a superheated state (*e.g.* in this case, water vapour at temperature over 100°C). To achieve this, a density–based solver is required, Fluent (2006). Here, a pressure–based solver is utilised to simulate accurately the interface between water and air. Moreover, when the real gas model is used, all fluid zones must contain real gas. Finally, the gas of interest is air at normal ambient conditions containing some degree of water vapour. Hence, the gas phase is humid air in equilibrium. For these reasons, calculations for real gas inside an OWC cannot be undertaken using the real gas tool of FLUENT®. Thus, a new gas with different density, specific heat at constant pressure and molar weight, following the results of the real gas model, is inserted as the gaseous phase of the numerical flume. This gas then behaves as a mixture of dry air and water vapour. It is not a real gas, but the approach offers a useful tool by which to compare against the results of the theoretical model. Humid air characteristics

are set following the theoretical model developed in previous sections, as shown in table 3.

	Dry air	Humid air
ρ	$1.225\,\mathrm{kg/m^3}$	$1.19\,\mathrm{kg/m^3}$
C_p	$1006.43\,\mathrm{J/kg{\cdot}K}$	$1503.70\,\mathrm{J/kg{\cdot}K}$
M	$28.966\,\mathrm{g/mol}$	$21.4\,\mathrm{g/mol}$

Table 3: Dry and humid air characteristics.

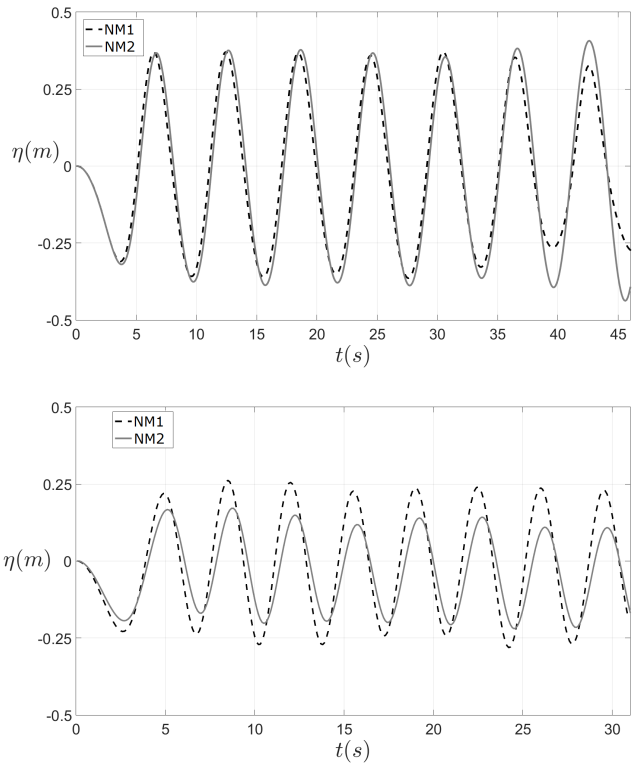

Figure 3: Free surface elevation time histories at generation gauge ($x = 12\,\mathrm{m}$) for humid and dry air conditions. $H = 1\,\mathrm{m}$, $T = 6\,\mathrm{s}$ (top); $H = 0.5\,\mathrm{m}$, $T = 3.5\,\mathrm{s}$ (bottom).

Fig. 3 shows the free surface elevation time histories obtained in both dry and humid tests at the gauge closest to the wave generator ($x = 12\,\mathrm{m}$) for two sets of wave conditions. Fig. 4 presents the free surface elevation time history inside the OWC chamber ($x = 120\,\mathrm{m}$). It can be seen that the free surface elevation time series predicted using the humid air model (NM2), and dry air model (NM1) are nearly the same at the generation gauge for the first case ($H = 1\,\mathrm{m}$, $T = 6\,\mathrm{s}$). Some discrepancies start to appear

near $t = 40\,\mathrm{s}$. Given that the OWC is located at the end of the flume, at $x = 120\,\mathrm{m}$, and noting that the wave speed would be about $6\,\mathrm{m/s}$, the initial wave crest takes about $17\,\mathrm{s}$ to arrive at the OWC, and $15\,\mathrm{s}$ to return back to the generation gauge, located at $x = 12\,\mathrm{m}$, after reflection. Hence, reflection effects are experienced by the OWC after $32\,\mathrm{s}$.

In the second case considered in Fig. 3 ($H = 0.5\,\mathrm{m}$, $T = 3.5\,\mathrm{s}$), there are substantial differences between the waveform generated for dry and humid conditions. These discrepancies are caused by viscous effects: the value of viscosity was not altered in this case, although it should have been modified to be consistent with the variations in specific heat, molar weight and density. Moreover, as the wave height is relatively small, viscous effects become more relevant. Despite this discrepancy, viscosity was not changed in the analytical real gas model (AM2) in order to be consistent. This provides a useful check by which to verify the accuracy of AM2.

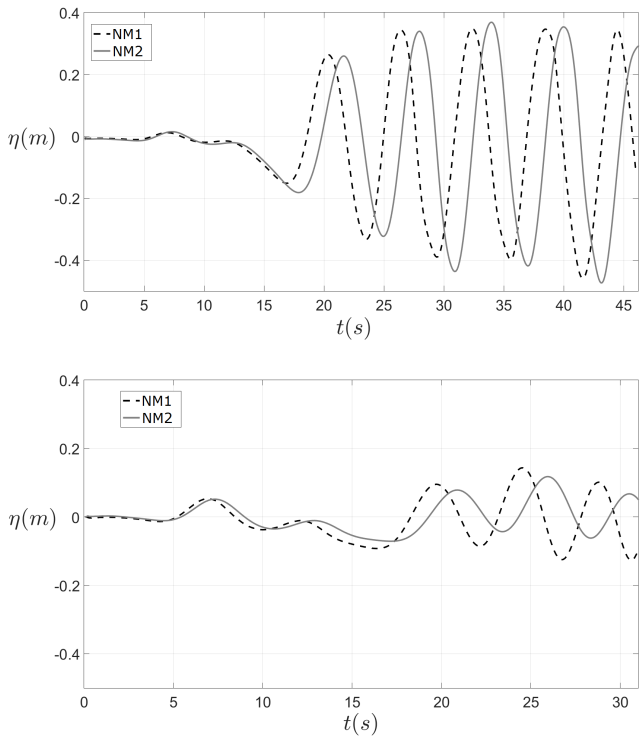

Figure 4: Free surface elevation time histories inside the OWC for humid and dry air conditions. $H = 1\,\mathrm{m}$, $T = 6\,\mathrm{s}$ (top); $H = 0.5\,\mathrm{m}$, $T = 3.5\,\mathrm{s}$ (bottom).

Fig. 4 shows that a phase difference occurs in the free surface motion inside the OWC chamber when humidity is taken into account. The phase difference affects the radiated and reflected waves. However, the variation is likely to be larger than would actually occur because of the inviscid fluid assumptions in the present FLUENT® model, which neglects the effect of viscosity on the flow, and which might be affected by the new air

conditions, Fluent (2006). The assumption of inviscid flow is valid if inertial forces dominate over fluid viscous forces, and is likely to be valid as a first approach. Turning to the free surface elevation time history inside the OWC for $H = 0.5\,\mathrm{m}$, $T = 3.5\,\mathrm{s}$, the results present a similar phase difference as observed for the $H = 1\,\mathrm{m}$, $T = 6\,\mathrm{s}$ case.

The scatter of pressure–air flow value about the trend line is very small for humid conditions (see Fig. 5). Whereas the $\Delta p - Q$ curve slope is the same for both dry and humid conditions, the extent of the humid case is lower than for the dry case. This affects power output, which is calculated as a function of pressure drop and air flow, meaning that power is lower in humid conditions, because both pressure and air flow are reduced.

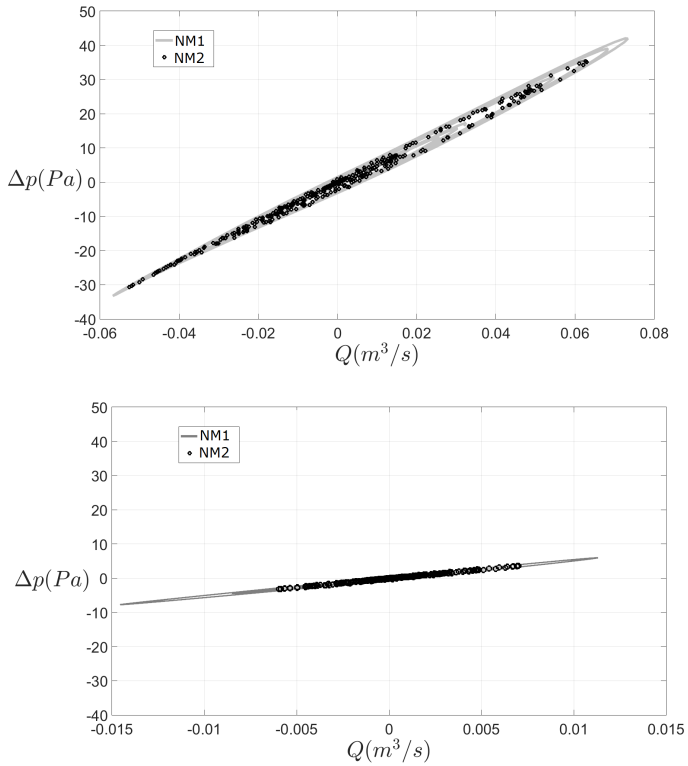

Figure 5: Pressure drop dependence on air flow rate inside OWC for humid and dry air conditions. $H = 1\,\mathrm{m}$, $T = 6\,\mathrm{s}$ (top); $H = 0.5\,\mathrm{m}$, $T = 3.5\,\mathrm{s}$ (bottom).

Fig. 6 shows the available power time histories, again comparing ideal and real gas models. It is evident that slight differences in pressure drop make a big difference in power output. For $H = 0.5\,\mathrm{m}$, $T = 3.5\,\mathrm{s}$, a large discrepancy is observed between dry and humid conditions. It should be noted that, although viscosity–induced differences lead to a notable variation in power output, this variation would have been much smaller if an accurate value for air viscosity had been available.

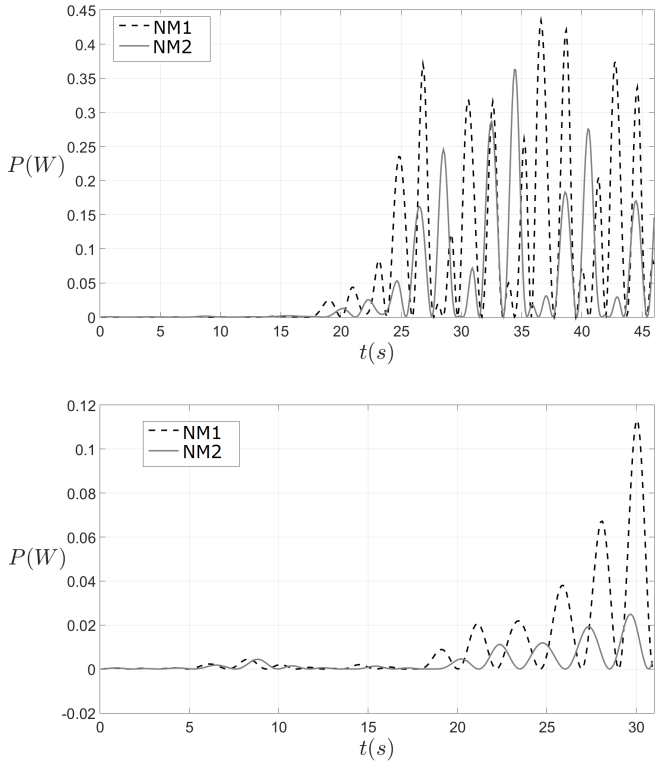

Figure 6: Available power time histories at turbine for humid and dry air conditions. $H = 1\,\mathrm{m}$, $T = 6\,\mathrm{s}$ (top); $H = 0.5\,\mathrm{m}$, $T = 3.5\,\mathrm{s}$ (bottom).

5. Comparison of analytical and numerical models

In this section, comparison is made between the numerical predictions from NM1 (dry conditions) and NM2 (humid conditions), and the analytical real gas model (AM2) developed by Medina-Lopez *et al.* (2017–II). As the pressure and adiabatic coefficient equations form a set of implicit equations, an initial value is needed to solve the system. Pressure results obtained from NM1 in FLUENT® are inserted into AM2. This way, we can see how the real gas analytical model (AM2) modifies ideal results from NM1, and then compare them with the results from NM2. The proposed methodology is summarised in Fig. 7.

Given that tests presented in this section are run for several waves (a sea state), the results are inherently different to those obtained by Medina-Lopez *et al.* (2017–II) over an ideal single wave cycle. This is primarily due to the application of a dynamic model instead of a standing wave model where the free surface elevation is in phase with the theoretical pressure. For an ideal sinusoidal signal, the power ratio between the ideal and real gas models is about 95 % (see section 6). However, the 2D numerical simulations enable more realistic wave conditions to be analysed, taking into account changing

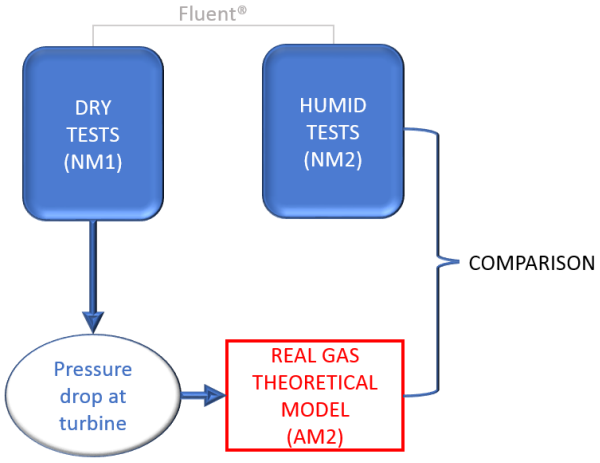

Figure 7: Proposed working procedure to obtain real gas pressures using the analytical model.

radiation and diffraction phenomena, which were considered constant throughout the preceding analysis. Moreover, the energy calculations carried out in the numerical solver take into account heat exchange. Using the virial formulation, the real gas model is specified to take into account inter-molecular interactions which are ignored in the ideal gas model. That said, a much bigger difference between the results using real and ideal formulations is expected for long–term or life–cycle analysis.

Fig. 8 shows the pressure variations in time obtained using NM2, and AM2. Fig. 8 left presents the raw data which exhibit a phase difference. It should be noted that the AM2 results are in phase with these from the ideal dry air numerical model (NM1). The pressure–adiabatic index system strongly depends on the specified initial values. Although variations in pressure magnitude are accounted for, the phase does not match the expected results. To compare values more effectively the numerical results are translated 2 s in Fig. 8 right, where the two curves almost overlap. The same procedure is followed for the second wave conditions ($H = 0.5\,\mathrm{m}$, $T = 3.5\,\mathrm{s}$) as shown in Fig. 9. In this case, slightly better agreement is obtained. Although the surface elevation time series differ for dry and humid numerical cases, viscous effects are more relevant for smaller waves, making inhalation and exhalation phenomena nearly symmetrical. As the present formulation only simulates the inhalation phase, the theoretical real gas simulation will be closer to the actual phenomena for smaller waves.

Fig. 10 shows the predicted available power time series at the OWC turbine using NM1 (dry air, numerical), NM2 (humid air, numerical), and AM2 (analytical real gas model). The power peaks are higher for NM1. In general, the behaviour of NM2 and AM2 power series is similar, although NM2 presents some higher peaks that are not present in the analytical approach. AM2 merely represents the inhalation phase, and so the higher peaks are not obtained. The lower figure supports the hypothesis that AM2 fits better smaller waves, where the inhalation and exhalation phases are symmetric. Moreover,

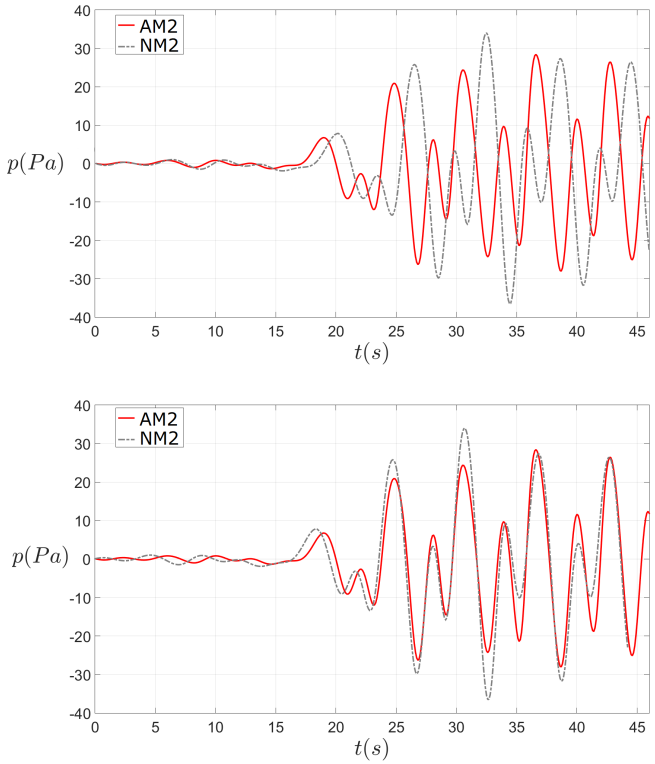

Figure 8: Pressure–time series inside OWC chamber for numerical tests using the humid air model (NM2), and the analytical real gas model (AM2). $H = 1\,\mathrm{m}$, $T = 6\,\mathrm{s}$. Raw time series (top), shifted time series (bottom).

the analytical model depends predominantly on changes in specific heat and density when the waves are smaller. For larger–scale waves, dynamic phenomena rule the wave behaviour, increasing the difference between predictions by the real gas analytical model and numerical simulations. Power values are smaller than expected due to the effects of viscosity. However, the analytical model provides results in very good agreement with its numerical counterpart. Given that the values are consistent, it is reasonable to conclude that both models, NM2 and AM2, can be used to simulate OWC real working conditions.

In terms of energy, Fig. 11 presents cumulative available energy at the turbine for the three cases. It is readily observed that the predictions by model NM1 are far from those of models NM2 and AM2. The NM2 and AM2 predictions are similar, although differences appear to grow in time. Table 4 lists the values of energy ratio obtained for the different tests. Although an energy ratio of about 50% is observed between AM2 and NM1, slightly different values are obtained for NM2. For frequencies away from $0.9\,\mathrm{Hz}$ (*i.e.* $T = 7\,\mathrm{s}$), discrepancies are observed between both numerical cases (NM1 and NM2). At $0.9\,\mathrm{Hz}$, the difference between the NM2 and AM2 results is a maximum, but the NM1 and NM2 results are almost equal. This might be due to resonance in the device.

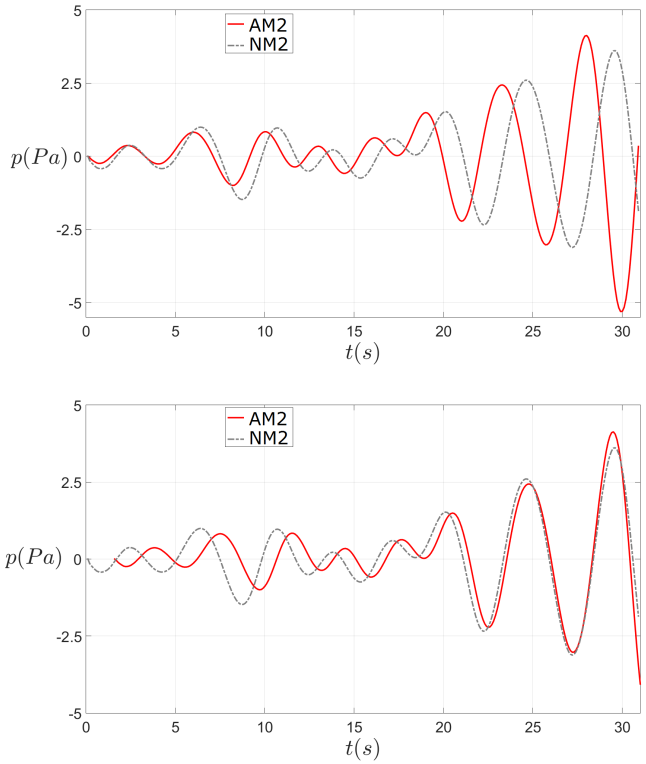

Figure 9: Pressure–time series inside OWC chamber for numerical tests using the humid air model (NM2), and the analytical real gas model (AM2). $H = 0.5\,\mathrm{m}$, $T = 3.5\,\mathrm{s}$. Raw time series (top), shifted time series (bottom).

Energy extraction by the device reaches a maximum at a frequency of about 0.9 Hz, as observed by Medina-Lopez *et al.* (2017–II). Maximum energy extraction for the device analysed is observed at about $kh = 0.4$, which corresponds to a period of $T \simeq 7\,\mathrm{s}$. In the resonance case, other phenomena can probably be ignored. However, at frequencies away from resonance the real gas model is more relevant.

The energy ratio between the analytical model and NM1 (dry case) is very stable, and is independent of wave conditions. The radiation–diffraction coefficients and the pressure drop change for every test, and so it is very likely that the underestimation of the real gas analytical model of about 50% of NM1 can be taken as a valid approach for the behaviour of the device under saturation conditions. This matches findings from the preliminary experiments, where the available power for the turbine tested under humid air conditions fell to an asymptotic value of about 40% (see Fig. 12. It should be noted that tests in FLUENT® were run for saturated conditions, $RH = 1$). In Fig. 12, the ratio between power under humid conditions and power in dry air conditions is plotted as a function of the relative humidity. Results from the experimental work apply to the

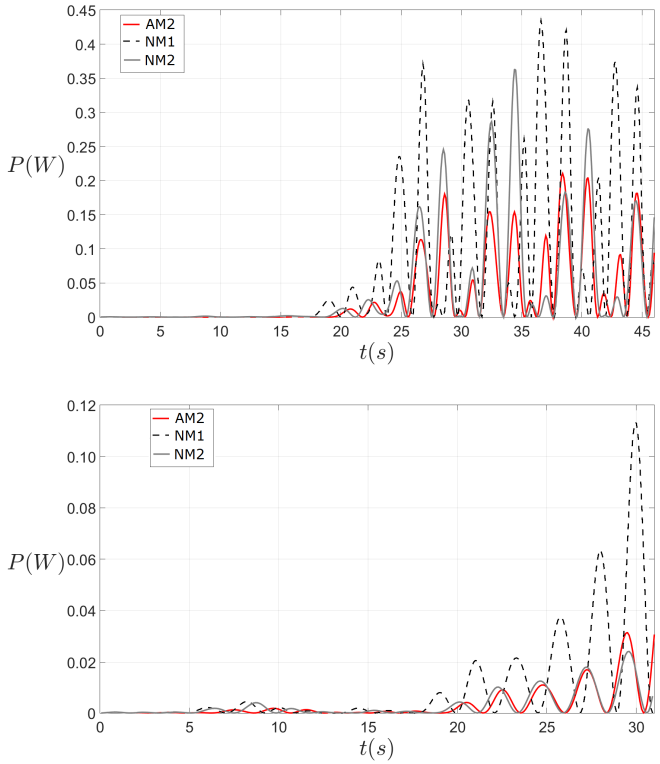

Figure 10: Available power time series at OWC turbine obtained using the numerical dry air model (NM1), numerical humid air model (NM2), and analytical real gas model (AM2): $H = 1\,\mathrm{m}$, $T = 6\,\mathrm{s}$ (top); $H = 0.5\,\mathrm{m}$, $T = 3.5\,\mathrm{s}$ (bottom).

specific laboratory conditions, but the similarity with the real gas model results provides confidence in the method.

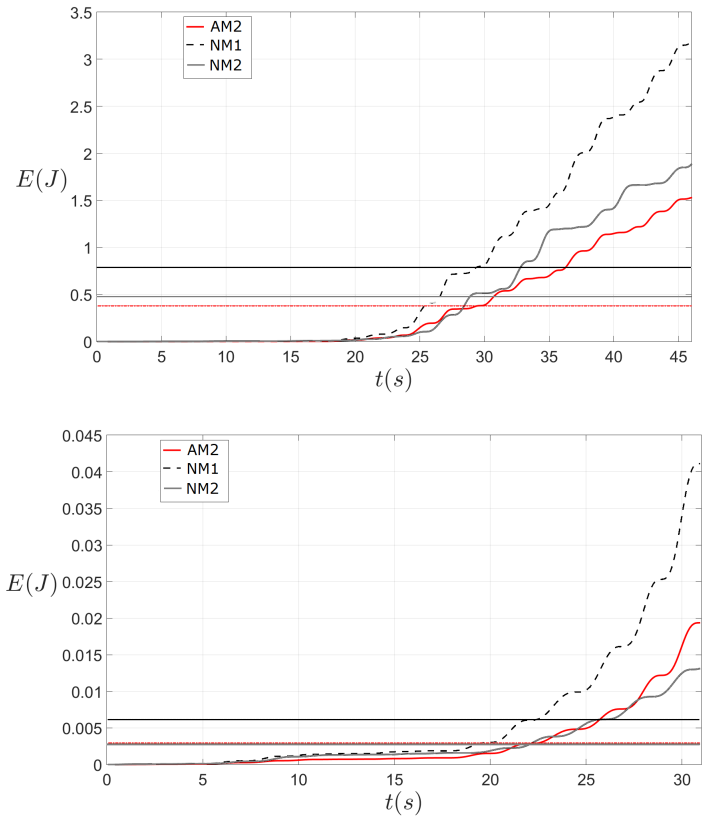

Figure 11: Cumulative energy time series, and mean energy at OWC turbine obtained using the numerical dry air model (NM1), numerical humid air model (NM2), and analytical real gas model (AM2): $H = 1\,\mathrm{m}$, $T = 6\,\mathrm{s}$ (top); $H = 0.5\,\mathrm{m}$, $T = 3.5\,\mathrm{s}$ (bottom).

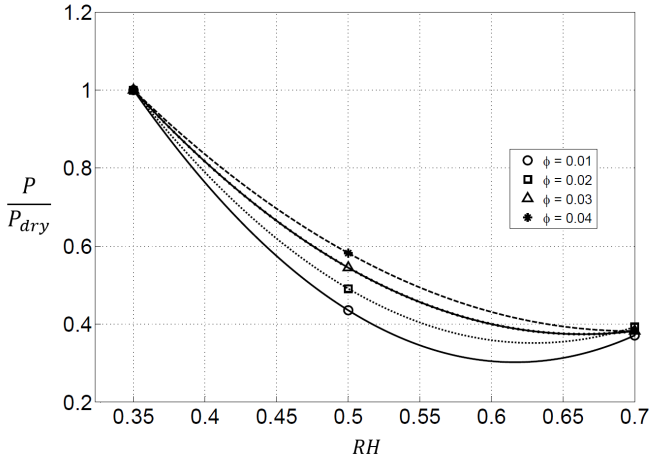

Figure 12: Power input ratio (humid air power over dry air power) as a function of relative humidity. [Source: Medina-Lopez *et al.* (2016)]

Test	E_{NM2}/E_{NM1}	E_{AM2}/E_{NM1}	E_{AM2}/E_{NM2}
$H = 0.5\,\mathrm{m}$, $T = 3.5\,\mathrm{s}$	0.3879	0.4763	1.1902
$H = 1\,\mathrm{m}$, $T = 6\,\mathrm{s}$	0.6146	0.4803	0.7748
$H = 1.5\,\mathrm{m}$, $T = 7\,\mathrm{s}$	1.0522	0.4821	0.4462
$H = 2\,\mathrm{m}$, $T = 8\,\mathrm{s}$	0.8204	0.4716	0.5748

Table 4: Ratios between estimated cumulative energy output obtained using dry numerical, humid numerical, and real analytical models.

5.1. Techno–economic discussion: implications for device design and cost of energy. A case study.

Following the cost estimations presented by de Andres et al. (2017), the maximum capital cost of an OWC would be around 4M€/MWh. Our findings indicate the Levelised Cost of Energy (LCOE) of an OWC will increase, as the accurate estimation of power with humid air is lower that for dry air. In order to make OWC devices competitive, a further reduction on LCOE is needed. Assuming the produced power reaches a limit, the focus is then on reducing the capital and operational expenditures of the device. This reduction can be achieved following two methods:

- Reducing the device operational life, and assuming easily replaceable elements in the design.
- Reducing the over–sizing of elements to reduce capital expenditures.

As presented by de Andres et al. (2017), the most relevant cost centre for OWCs is the device structure, which typically implies considerable prime movers and use of material. In practical terms, the inclusion of real gas theory in the design stage of OWC wave energy converters will impact their LCOE significantly. The accurate estimation in Annual Energy Production (AEP) will initially increase the LCOE, but should also lead to the re–engineering of the device to adapt to real gas conditions. As a simple calculation taking into account the results from real gas theory, if the real gas value of AEP is about 70 % of the ideal gas value of AEP, the LCOE will increase by a factor of 1.4. This factor should be applied to reduce CAPEX and OPEX in order to keep the OWC competitive. Sensitivity to changes in expected AEP is very important, because for every 1 % reduction in energy production from the ideal gas scenario, the cost of energy would increase 1 %, assuming expenditure remains constant in both cases. Reducing expenditure to keep a low cost of energy is a demanding goal, but it could be achieved by developing devices with adaptable resonance frequencies depending on the wave conditions to help mitigate the real gas effects, reducing operational costs. In order to reduce risk and capital costs, the adaptable frequency OWC should be smaller, and in order to increase AEP, this new concept of OWCs should be part of multi–device farms that could potentially be located anywhere in the world.

In fact, a lower cost of energy might be achieved by focusing on the fact that lower efficiency values can be positively balanced if lower cost and performance devices are considered. Let us consider the case of the Spanish coast, where the wave energy resource along its 8000 km is estimated as $3 \sim 5\,\mathrm{kW/m}$ when harvested in shallow waters, and

497 $10 \sim 15\,\mathrm{kW/m}$ for off–shore harvesting, Heras–Saizarbitoria *et al.* (2013). In order
498 to explain the general aspects commented above, a site is selected along the Spanish
499 Mediterranean coast representative of a moderate wave climate condition (Carchuna
500 coast, Granada, southern Spain). Whereas climate studies for Mediterranean sites reveal
501 mild energetic wave conditions, Stefanakos et al. (2004), some authors have shown that
502 OWC devices can render a better or even optimal performance under waves of peak
503 periods around $\simeq 6 \sim 7\,\mathrm{s}$, Jalón *et al.* (2016). In the case of Carchuna, the significant
504 wave height H_{m0} for wave climate time series for the period 1997–2013 (SIMAR spot
505 2042079, Spanish Government Ports Authority) and the corresponding peak periods T_z
506 are represented in Fig. 13 and Fig. 14 respectively. From the statistical analysis it is
507 deduced that sea states with $0.5 \leqslant H_{m0} \leqslant 2\,\mathrm{m}$ (highlighted in green) and peak periods
508 around $7\,s$ have a recurrence period of $\simeq 3000$ hours per year, while sea states above that
509 threshold (highlighted in cyan) have a recurrence of $\simeq 100$ hours.

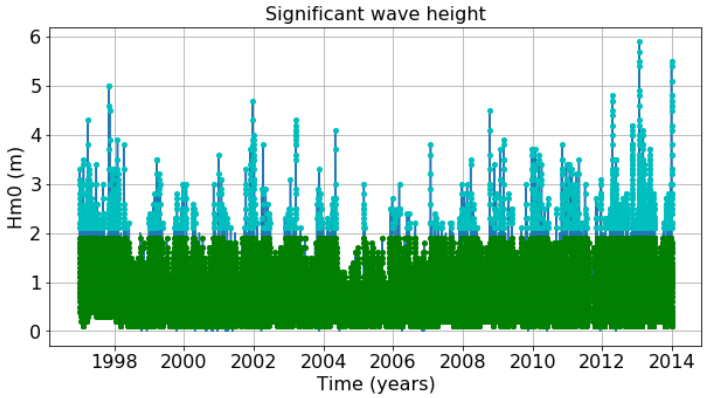

Figure 13: Significant wave height H_{m0} for a Spanish south coast site (Carchuna beach, Granada). Wave heights under 2 m plotted in green.

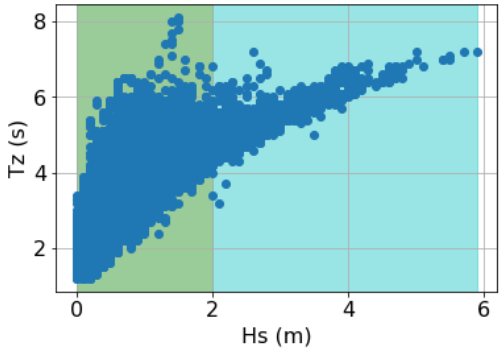

Figure 14: Peak periods T_z for a Spanish south coast site (Carchuna beach, Granada). Values associated to wave heights under 2 m higlighted in green.

510 Consider two hypothetical OWC installation set up alternatives for the specified

location, one for a production of 10 kW and another one for 1000 kW. Capital costs of 0.01 MW $\times$4M€/MWh and 1 MW $\times$4M€/MWh respectively would be assigned according with installation power. However, a first reduction on capital would be feasible from implementation of real gas calculations for expected efficiency which leads to reduced power input (in certain case up to $\simeq$ 70 %, see Fig. 12), hence a reduction in the required installed power and in the associated costs. In addition, noting that moderate climate conditions can lead to a better efficiency of the device, a low production set up with a low cost design and deployment might lead to a more profitable installation in the mid- and long–term. For this example the 10 KW set up, which could be oriented to exploit the mild climate conditions, would provide an annual average of $\simeq 3000 \times 10 =$ 30000 kWh transformed and delivered to the grid, and the 1000 kW set up would deliver $\simeq$ 100000 kWh. These rough estimates reveal that the low production set up has an overall cost 100 times below the high production set up; however, the difference in energy production is only 3.3 times below that of the higher production set up. The foregoing discussion is by itself a future research line in which the techno–economical optimization of simple OWC devices is the main goal. Nevertheless, the calculation highlights the fact that a feasible way to bridge the gap between design, deployment and efficient use of the technology would be to advance the design of low cost devices, so that they are more adaptable to mild climates in terms of efficiency, easier to maintain and to replace.

6. Conclusions

This paper has included humidity effects through a real gas model of an OWC coupled to hydrodynamic radiation–diffraction. The changing nature of the adiabatic coefficient n implies that the system presents hysteresis related to the compression and expansion processes following different adiabatic curves. Given that adiabatic curves within the same p–V diagram do not intersect, the system then moves in a third dimension: temperature. Here, the hysteresis is related to the system changing to a different temperature than that at the end of the adiabatic process. During a period of time between two adiabatic processes, heat exchange with the surroundings might be allowed, changing the overall temperature of the system. The concept can be observed in Fig. 15, which shows the p–V–T conditions of the process. The different adiabatic curves available are plotted in green in the left panel. In defining the cycle within the OWC, it is assumed there is a compression process and an expansion process, probably linked by two processes at constant temperature: condensation and evaporation. The hysteresis of the processes makes consecutive cycles inside the chamber displace in p–V–T space. This hysteresis might be caused by differences between consecutive adiabatic processes within a compression–expansion cycle.

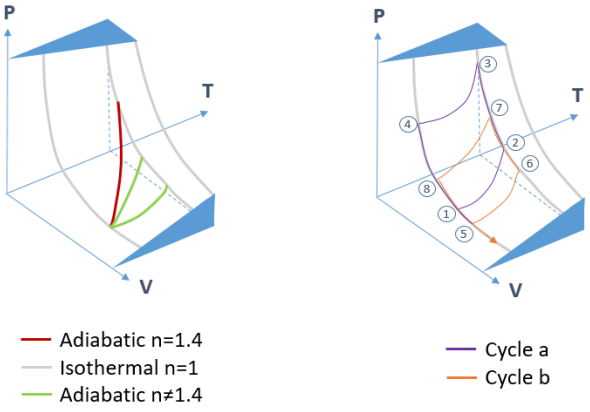

Figure 15: Pressure–volume–temperature (p–V–T) diagrams showing different types of curves analysed(left), and different cycle paths inside the OWC chamber (right).

When comparing the numerical results with those from the analytical real gas model, several discrepancies are evident. The discrepancy in phase may have been caused by the initial pressure values taken for iteration, and is worth further investigation. It should be noted that FLUENT® applies an ideal gas model for a mix of dry air and water vapour whereas the analytical model applies a real gas model. The real gas model is likely to be more accurate than a mix of two ideal gases, because it represents inter–molecular forces and heat exchange.

An index of the relative energy extraction predicted by real and ideal gas models is given by the ratio of the areas under the corresponding power curves (see Fig. 10). This index is almost 70 % for the humid air model (NM2) compared with the dry air model (NM1), and 50 % for the analytical real gas model (AM2) compared with the dry air model (NM1). In other words, the ratio between the energies predicted by AM2 and NM2 is about 80 %. This finding can be applied at frequencies different to that of resonance of the device, where both numerical models are almost equivalent. However, the index of relative cumulative energy extracted between the analytical real gas model and the dry air numerical model is almost constant at about 50 % over the range of cases studied. The differences between real and ideal gas approaches should be analysed further at frequencies close to resonance.

Future numerical and analytical studies are recommended as follows. Development of a real gas numerical model at standard temperature and pressure conditions would enable validation of the present analytical model. The resulting numerical model should be coupled with a suitable wave model, such as *waves2foam* in *OpenFOAM*, as well as a compressible solver for the air phase in future models. Physical model tests investigating different temperature and humidity forcing conditions would be useful for validation purposes. Moreover, future analytical models should focus on the effects of condensation and evaporation, and droplet formation on turbine blades and in the OWC chamber.

Acknowledgements

The work of the first author was funded by the TALENTIA Fellowship Programme by the Regional Ministry of Economy, Innovation, Science and Employment in Andalusia (Spain). The authors wish to thank Professor María Clavero of the Andalusian Institute for Earth System Research, Universidad de Granada, for sharing her expertise in wave climate.

References

Cruz J., 2008. *Ocean Wave Energy. Current Status and Future Perspectives*. Springer–Verlag. 431 p.p. I.S.B.N. 978 − 3 − 540 − 74894 − 6.

Falcão A. F. de O., 2010. *Wave Energy Utilization: A Review of Technologies*. Renewable and Sustainable Energy Reviews, Vol. 14, pp. 899–918.

Gato L. M. C. & Falcão A. F. de O., 1984 *On the Theory of the Wells Turbine*. Transactions of the ASME, Vol.106, pp. 628–633.

Raghunathan S., 1995. *The Wells Turbine for Wave Energy Conversion*. Prog. Aerospace. Sci., Vol. 31, pp. 335–386.

SI Ocean Energy Project, 2013. *Ocean Energy: State of the Art*. Strategic Initiative for Ocean Energy. http://www.si-ocean.eu/en/Home/Home/

SI Ocean Energy Project, 2013. *Ocean Energy: Cost of Energy and Cost Reduction Opportunities*. Strategic Initiative for Ocean Energy. http://www.si-ocean.eu/en/Home/Home/

SI Ocean Energy Project, 2013. *Ocean Energy: Gaps and Barriers*. Strategic Initiative for Ocean Energy. http://www.si-ocean.eu/en/Home/Home/

Heras–Saizarbitoria I., Zamanillo I. & Laskurain I., 2013. *Social Acceptance of Ocean Wave Energy: a Case Study of an OWC Shoreline Plant*. Renewable and Sustainable Energy Reviews, Vol. 27, pp. 515–524.

Hitzeroth M. & Megerle A., 2013. *Renewable Energy Projects: Acceptance Risks and their Management*. Renewable and Sustainable Energy Reviews, Vol. 27, pp. 576–584.

Magagna D. & Uihlein A., 2015. *Ocean Energy Development in Europe: Current Status and Future Perspectives*. International Journal of Marine Energy, Vol. 11, pp. 84–104.

Evans D. V., 1982. *Wave Power Absorption by Systems of Oscillating Pressure Distributions*. Journal of Fluid Mechanics, Vol. 114, pp. 481–499.

Sarmento A. J. N. A. & Falcão A. F. de O., 1985. *Wave Generation by an Oscillating Surface–Pressure and its Application in Wave–Energy Extraction*. Journal of Fluid Mechanics, Vol. 150, pp. 467–485.

Evans D. V. & Porter R., 1995. *Hydrodynamic Characteristics of an Oscillating Water Column Device*. Applied Ocean Research, Vol. 17, pp. 155–164.

Martins–Rivas H. & Mei C. C., 2009. *Wave Power Extraction from an Oscillating Water Column at the Tip of a Breakwater*. Journal of Fluid Mechanics, Vol. 626, pp. 395–414.

Martins–Rivas H. & Mei C. C., 2009. *Wave Power Extraction from an Oscillating Water Column along a Straight Coast*. Ocean Engineering, Vol. 36, pp. 426–433.

Lovas S., Mei C. & Liu Y., 2010. *Oscillating Water Column at a Coastal Corner for Wave Power Extraction*. Applied Ocean Research, Vol. 32, pp. 267–283.

Gato L. M. C. & Falcão A. F. de O., 1989 *Aerodynamics of the Wells Turbine: Control by Swinging Rotor Blades*. International Journal of Mechanical Science, Vol.31 (6), pp. 425–434.

Justino P. A. P. and Falcão A. F. de O., 1999. *Rotational Speed Control of an OWC Wave Power Plant*. Journal of Offshore Mechanics and Arctic Engineering. ASME, Vol.121, pp. 65–70.

Falcão A. F. de O. & Justino P. A. P., 1999. *OWC Wave Energy Devices with Air Flow Control*. Ocean Engineering, Vol. 26, pp. 1275–1295.

Falcão A. F. de O., Henriques J. C. C. & Gato L. M. C., 2016. *Rotational Speed Control and Electrical Rated Power of an Oscillating-Water-Column Wave Energy Converter*. Energy, Vol. 120, pp. 253–261.

López. I., Pereiras B., Castro F. & Iglesias G., 2014. *Optimisation of Turbine-Induced Damping for an OWC Wave Energy Converter using a RANS-VOF Numerical Model*. Applied Energy, 127, pp. 105–114.

López. I., Pereiras B., Castro F. & Iglesias G., 2015. *Performance of OWC Wave Energy Converters: Influence of Turbine Damping and Tidal Variability*. International Journal of Energy Research, 39, 4, pp. 472–483.

Zhang Y., Zou Q. P. and Greaves D.M., 2012. *Air water Two–Phase Flow Modelling of Hydrodynamic Performance of an Oscillating Water Column Device*. Renewable Energy, Vol. 49, pp. 159–170.

Rezanejad K., Bhattacharjee J. & Guedes Soares C., 2013. *Stepped Seabottom Effects on the Efficiency of Nearshore Oscillating Water Column Device*. Coastal Engineering, Vol. 70, pp. 25–38.

Rezanejad K., Bhattacharjee J. & Guedes Soares C., 2015. *Analytical and Numerical Study of Dual-Chamber Oscillating Water Columns on Stepped Bottom*. Renewable Energy, Vol. 75, pp. 272–282.

Medina–López E., Bergillos R. J., Moñino A., Clavero M. & Ortega–Sánchez M., 2017. *Effects of Seabed Morphology on Oscillating Water Column Wave Energy Converters*. Energy, Vol. 135, pp. 659–673.

Medina–López E., Bergillos R.J., Moñino A., Clavero M. & Ortega-Sánchez M., 2018. *The influence of storm evolution on the performance of Oscillating Water Columns*. Energy, *Under revision*.

Mendoza E., Dias J., Didier E., Fortes C. J. E. M., Neves M. G., Reis M. T., Conde J. M. P. Poseiro P & Teixeira P. R. F., 2017. *An Integrated Tool for Modelling Oscillating Water Column (OWC) Wave Energy Converters (WEC) in Vertical Breakwaters*. Journal of Hydro-environment Research, http://dx.doi.org/10.1016/j.jher.2017.10.007.

Jalón M. L., Baquerizo A. & Losada M. A., 2016. *Optimization at Different Time Scales for the Design and Management of an Oscillating Water Column System*. Energy, Vol. 95, pp. 110–123.

Teixeira P., Davyt D., Didier E. & Ramalhais R., 2013. *Numerical Simulation of an Oscillating Water Column Device Using a Code Based on Navier–Stokes Equations*. Energy, 61, pp. 513–530.

Luo Y., Nader J. R., Cooper P. & Zhu S. P., 2014. *Nonlinear 2D Analysis of the Efficiency of Fixed Oscillating Water Column Wave Energy Converters*. Renewable Energy, Vol. 64, pp. 255–265.

Moñino A., Medina–López E., Clavero M. & Benslimane S., 2017. *Numerical simulation of a simple OWC problem for turbine performance*. International Journal of Marine Energy, 20, pp. 17–32.

Iturrioz A., Guanche R., Lara J. L., Vidal C. & Losada I. J., 2015. *Validation of OpenFOAM for Oscillating Water Column Three-Dimensional Modeling*. Ocean Engineering, Vol. 107, pp. 222–236.

Rezanejad K., Guedes Soares C., López I & Carballo R. 2017. *Experimental and Numerical Investigation of the Hydrodynamic Performance of an Oscillating Water Column Wave Energy Converter*. Renewable Energy, Vol. 106, pp. 1–16.

Bingham H. B., Ducasse D., Nielsen K. & Read R., 2015 *Hydrodynamic Analysis of Oscillating Water Column Wave Energy Devices*. Journal of Ocean Engineering & Marine Engineering, DOI 10.1007/s40722–015–0032–4.

673 Elhanafi A., Macfarlane G., Fleming A. & Leong Z., 2017. *Scaling and Air*
674 *Compressibility Effects on a Three-Dimensional Offshore Stationary OWC Wave Energy*
675 *Converter*. Applied Energy, Vol. 189, pp. 1–20.
676 Sheng W., Alcorn R., & Lewis S., 2013. *On Thermodynamics of Primary Energy*
677 *Conversion of OWC Wave Energy Converters*. Renewable Sustainable Energy, 5, 023105.
678 Medina–López E., Moñino A., Clavero M., Del Pino C. & Losada M. A., 2016. *Note*
679 *on a Real Gas Model for OWC Performance*. Renewable Energy, Vol. 85, pp. 588–597.
680 Prausnitz J., Lichtenthaler R. & Gomes de Azevedo E., 1999. *Molecular Thermody-*
681 *namics of Fluid–Phase Equilibria*. Prentice–Hall. 864 pp. i.s.b.n. $0-13-977745-8$
682 Wisniak J., 2003. *Eike Kamerlingh–The Virial Equation of State*. Indian Journal of Chemical
683 Technology, Vol. 10, pp. 564–572.
684 Tsonopoulos C. & Heidman J. L., 1990. *From the Virial to the Cubic Equation of State*.
685 Fluid Phase Equilibria, Vol. 57, pp. 261–276.
686 Medina–López E., Moñino A., Borthwick A. G. L. & Clavero M., 2017. *Thermody-*
687 *namics of an OWC Containing Real Gas*. Energy, Vol. 135, pp. 709–717.
688 O'Hagan A. M., Huertas C., O'Callaghan J. & Greaves D.M., 2016. *Wave Energy in*
689 *Europe: Views on Experiences and Progress to Date*. International Journal of Marine Energy,
690 Vol. 14, pp. 180–197.
691 National Ocean Economic Program (2017). *Off–Shore Renewable Energy*. `http://www.`
692 `oceaneconomics.org/offshore_renewables/costs/`
693 Jalón L, 2016. *Diseño óptimo de un sistema de aprovechamiento de la energía del oleaje y*
694 *gestión integral a diferentes escalas de tiempo. Optimal design of a wave energy converter and*
695 *integrated management at different time scales*. PhD Thesis. Universidad de Granada.
696 Fluent Inc., 2006. *FLUENT® 6.3 User's Guide*. Help `.pdf`. Fluent Inc., Centerra Resource
697 Park, 10 Cavendish Court, Lebanon, NH 03766. 2501 p.p.
698 de Andres A., Medina-Lopez E., Crooks D., Roberts O. & Jeffrey H., 2017. *On*
699 *the reversed LCOE calculation: design constraints for wave energy commercialization*.
700 International Journal of Marine Energy, 18, pp. 88–108, 2017.
701 Stefanakos C.N., Athanassoulis G.S.,Cavaleri L, Bertotti L. & Lefevre J.M.,
702 2004. *Wind and Wave Climatology of the Mediterranean Sea. Part II: Wave Statistics*.
703 Proceedings of the Fourteenth International Offshore and Polar Engineering Conference,
704 Toulon, France, May 23-28.

705 Appendix I: OWC classic formulation

In order to set appropriately the context and the scope of the study, a brief review of the classic OWC formulation is presented, as defined by Martins–Rivas & Mei (2009–I). If a Wells turbine – or any linear response turbine – is used for the power take-off system, the mass flow rate Q_T^m through the turbine can be defined in terms of the pressure drop in linear form:

$$Q_T^m = \rho Q_T = \frac{KD}{N} p \,, \tag{16}$$

706 where K depends on turbine parameters, D is turbine diameter, N is turbine rotation
707 velocity, and ρ is air density inside the OWC chamber.
708

The volumetric flow rate inside the OWC, Q_{owc}, can be expressed as:

$$Q_{owc} = \frac{KD}{N\rho} p + \frac{V}{C_s^2 \rho} \left(\frac{dp}{dt} \right) \,, \tag{17}$$

where C_s is the speed of sound in air.

Following Martins–Rivas & Mei (2009–I) and applying harmonic solutions, we obtain:

$$\widehat{Q}_{owc} = \frac{KD}{N\rho}\widehat{p} - i\omega\frac{V}{C_s^2\rho}\widehat{p}, \tag{18}$$

where both $\widehat{Q}_{owc}$ and $\widehat{p}$ are complex amplitudes defined in the classic problem.

If as discussed before a steady–state flow is considered, the continuity equation simply reads:

$$Q_{owc} = \frac{KD}{N\rho}p, \tag{19}$$

with Q_{owc} and p defined as real quantities. In general terms, the power input to the turbine is expressed as:

$$P = pQ_{owc}\,. \tag{20}$$

Following Martins–Rivas & Mei (2009–I), the average power $\overline{P}$ extracted from the pneumatic power inside the chamber is:

$$\overline{P} = \frac{1}{2}\frac{KD}{N\rho}|\widehat{p}|^2 = \frac{1}{2}\frac{KD}{N\rho}\frac{|\tilde{\Gamma}|^2(H/2)^2}{(\frac{KD}{N\rho}+\tilde{B})^2 + (\tilde{C}+\frac{\omega V}{C_s^2\rho})^2}\,, \tag{21}$$

and the capture length, understood as an efficiency expression, is:

$$kL = \frac{8k\overline{P}}{\rho_w g H^2 C_g} = \frac{gka}{\omega C_g}\frac{\chi|\tilde{\Gamma}|^2}{(\chi+\tilde{B})^2 + (\tilde{C}+\beta)^2}\,. \tag{22}$$

Coefficients $\tilde{B}$, $\tilde{C}$, $\tilde{\Gamma}$, χ and β are the mathematical representation of oscillation damping, restitution of the added mass, flow in the chamber associated with diffraction, and turbine characteristics. H is wave height, C_g is wave group celerity, $g = 9.81\,m/s^2$ is acceleration due to gravity, k is wave number, and a is the OWC radius.

Summarising:

$$\tilde{\Gamma} = \Gamma/\left(\frac{ag}{\omega}\right)\,, \tag{23}$$

$$\tilde{B} = B/\left(\frac{a}{\omega\rho_w}\right)\,, \tag{24}$$

$$\tilde{C} = C/\left(\frac{a}{\omega\rho_w}\right)\,, \tag{25}$$

$$\chi = \frac{\rho_w KD\omega}{\rho N a}\,, \tag{26}$$

and

$$\beta = \frac{\omega^2 V_0 \rho_w}{C_s^2 a\rho}\,. \tag{27}$$

Appendix II: Real gas pressure formulation development

6.1. Inhalation

For inhalation, an expression for pressure incorporating the effect of real gas is obtained by substituting (3) and (5) into (6). The governing equation is:

$$n\left(\frac{KD}{N\rho_0}-\frac{V}{p_0}\frac{d(1/n)}{dt}-i\frac{\omega V}{p_0 n}\right)\frac{p_0 p_g^{in}}{np_0+p_g^{in}}=-\left(\mathbb{B}-i\mathbb{C}\right)p_g^{in}+\Gamma A_0 \tag{28}$$

where $i=\sqrt{-1}$, and p_g^{in} is pressure of real gas in the inhalation part of the cycle. After rearranging using the *Matlab*® tool *Solve*, an implicit expression for p_g^{in} and n is obtained as:

$$\boxed{p_g^{in}=\begin{cases}\dfrac{A_0\,N\,\Gamma\,\rho_0\;-\;\alpha\;-\;D\,K\,n\,p_0\;+\;\zeta\;-\;\kappa\;+\;\varepsilon\;+\;\vartheta}{\psi}\\[2ex] \dfrac{A_0\,N\,\Gamma\,\rho_0\;+\;\alpha\;-\;D\,K\,n\,p_0\;+\;\zeta\;-\;\kappa\;+\;\varepsilon\;+\;\vartheta}{\psi}\end{cases}} \tag{29}$$

where

$$\begin{aligned}\alpha=[&N^2\,V^2\,\rho_0^2\,\omega^2\;-\;D^2\,K^2\,n^2\,p_0^2\;-\;A_0^2\,N^2\,\Gamma^2\,\rho_0^2\;-\;\mathbb{B}^2\,N^2\,n^2\,p_0^2\,\rho_0^2\\&+\mathbb{C}^2\,N^2\,n^2\,p_0^2\,\rho_0^2-\;N^2\,V^2\left(\frac{d(1/n)}{dt}\right)^2 n^2\,\rho_0^2\;+\;2\mathbb{B}\,N^2\,V\,\frac{d(1/n)}{dt}\,n^2\,p_0\,\rho_0^2\\&-2\mathbb{B}\,D\,K\,N\,n^2\,p_0^2\,\rho_0-\;2A_0\,\mathbb{B}\,N^2\,\Gamma\,n\,p_0\,\rho_0^2\;-\;2A_0\,N^2\,V\,\frac{d(1/n)}{dt}\,\Gamma\,n\,\rho_0^2\\&+2\mathbb{C}\,N^2\,V\,n\,p_0\,\rho_0^2\,\omega+\;2A_0\,D\,K\,N\,\Gamma\,n\,p_0\,\rho_0\;+\;2D\,K\,N\,V\,\frac{d(1/n)}{dt}\,n^2\,p_0\,\rho_0\\&+(\mathbb{B}\,\mathbb{C}\,N^2\,n^2\,p_0^2\,\rho_0^2-\;A_0\,N^2\,V\,\Gamma\,\rho_0^2\,\omega\;-\;N^2\,V^2\,\frac{d(1/n)}{dt}\,n\,\rho_0^2\,\omega\\&-\mathbb{C}\,N^2\,V\,\frac{d(1/n)}{dt}\,n^2\,p_0\,\rho_0^2+\;\mathbb{C}\,D\,K\,N\,n^2\,p_0^2\,\rho_0\;+\;A_0\,\mathbb{C}\,N^2\,\Gamma\,n\,p_0\,\rho_0^2\\&+\mathbb{B}\,N^2\,V\,n\,p_0\,\rho_0^2\,\omega\;+\;D\,K\,N\,V\,n\,p_0\,\rho_0\,\omega)\,2i]^{1/2}\,i\,,\end{aligned} \tag{30}$$

$$\psi=\left(\mathbb{B}N\rho_0-\mathbb{C}N\rho_0\,i\right)^2\,, \tag{31}$$

$$\varepsilon=\mathbb{C}Nnp_0\rho_0\,i\,, \tag{32}$$

$$\zeta=NV\rho_0\omega\,i\,, \tag{33}$$

$$\vartheta=NV\frac{d(1/n)}{dt}n\rho_0\,, \tag{34}$$

and

$$\kappa=\mathbb{B}Nnp_0\rho_0\,. \tag{35}$$

Equation (29) is solved iteratively using the Newton Method. The solution converges rapidly given a suitable initial value for pressure, after about the 6^{th} or 7^{th} iteration, with a relative error lower than 1%. Equation (29) provides two solutions for p_g^{in}, of which the upper is unphysical and the lower is valid.

It should be noted that if the initial airflow equations (3) and (4) were to be linearised a second time in terms of pressure–density relationship, the set of equations obtained for pressure would be exactly equivalent to those presented by Martins–Rivas & Mei (2009–I).

In the classical formulation, the local derivative of pressure with time is linearly related to the local derivative of density with time and the initial speed of sound in air. Using this simplification, an identical result is obtained to that using the linearised adiabatic relationship between density and pressure, provided the adiabatic index is constant. Our hypothesis is that the adiabatic conditions in the OWC chamber are time dependent, and so the rate of change of n with time has to be taken into account. A further simplification step is therefore needed to achieve the same results as given by the classical formulation.

6.2. Exhalation

For exhalation, an expression for pressure based on the real gas model is obtained by substituting (4) and (5) into (6). The resulting equation to solve is:

$$\frac{KD}{N\rho_g} - \frac{p_g^{ex} V \left(\dfrac{\partial(1/n)}{\partial t}\right)}{p_0 + p_g^{ex} e^{-i\omega t}} - i\frac{\omega V}{n\left(p_0 + p_g^{ex} e^{-i\omega t}\right)} = -\left(\mathbb{B} - i\mathbb{C}\right) p_g + \Gamma A_0 \tag{36}$$

Taking into account real gas in the exhalation part of the cycle, the pressure is given by

$$\boxed{p_g^{ex} = \begin{cases} -\dfrac{D\,K\,n\,p_0 \,+\, \tau \,+\, \zeta_g \,+\, \varsigma \,-\, \kappa_g \,+\, \varepsilon_g \,-\, \vartheta_g}{\varrho} \\ -\dfrac{D\,K\,n\,p_0 \,-\, \tau \,+\, \zeta_g \,+\, \varsigma \,-\, \kappa_g \,+\, \varepsilon_g \,-\, \vartheta_g}{\varrho} \end{cases},} \tag{37}$$

where

$$\tau = [-N^2\,V^2\,\rho_g^2\,\omega^2 \;+\; D^2\,K^2\,n^2\,p_0^2 \;+\; A_0^2\,N^2\,\Gamma^2\,n^2\,\rho_g^2 \tag{38}$$
$$+\,\mathbb{B}^2\,N^2\,n^2\,p_0^2\,\rho_g^2 - \;\mathbb{C}^2\,N^2\,n^2\,p_0^2\,\rho_g^2 \;+\; 2A_0\,\mathbb{B}\,N^2\,V\,\frac{d(1/n)}{dt}\,\Gamma\,n^2\,p_0\,\rho_g^2$$
$$+\,N^2\,V^2\,\left(\frac{d(1/n)}{dt}\right)^2\,n^2\,\rho_g^2 \;-2A_0\,N^2\,V\,\frac{d(1/n)}{dt}\,\Gamma\,n^2\,\rho_g^2$$
$$+\,2\mathbb{B}\,N^2\,V\,\frac{d(1/n)}{dt}\,n^2\,p_0\,\rho_g^2 \;-\; 2\mathbb{B}\,D\,K\,N\,n^2\,p_0^2\,\rho_g \;-\; 2\mathbb{C}\,N^2\,V\,n\,p_0\,\rho_g^2\,\omega$$
$$-\,2A_0\,D\,K\,N\,\Gamma\,n^2\,p_0\,\rho_g \;-\; 2D\,K\,N\,V\,\frac{d(1/n)}{dt}\,n^2\,p_0\,\rho_g \;+\; (-\mathbb{B}\,\mathbb{C}\,N^2\,n^2\,p_0^2\,\rho_g^2$$
$$-\,N^2\,V^2\,\frac{d(1/n)}{dt}\,n\,\rho_g^2\,\omega \;-\; A_0\,\mathbb{C}\,N^2\,\Gamma\,n^2\,p_0\,\rho_g^2 \;-\; \mathbb{C}\,N^2\,V\,\frac{d(1/n)}{dt}\,n^2\,p_0\,\rho_g^2$$
$$+\,\mathbb{C}\,D\,K\,N\,n^2\,p_0^2\,\rho_g \;+\; A_0\,N^2\,V\,\Gamma\,n\,\rho_g^2\,\omega \;-\; \mathbb{B}\,N^2\,V\,n\,p_0\,\rho_g^2\,\omega$$
$$+\,D\,K\,N\,V\,n\,p_0\,\rho_g\,\omega)\,2i]^{1/2}\,,$$

$$\varrho = (DKn - \mathbb{B}Nn\rho_g + \mathbb{C}Nn\rho_g\,i)^2\;, \tag{39}$$

$$\varepsilon_g = \mathbb{C}Nnp_0\rho_g\,i\,, \tag{40}$$

$$\zeta_g = NV\rho_g\omega\,i\,, \tag{41}$$

$$\vartheta_g = NV\frac{d(1/n)}{dt}n\rho_g\,, \tag{42}$$

$$\kappa_g = \mathbb{B}Nnp_0\rho_g\,, \tag{43}$$

and

$$\varsigma = A_0N\Gamma n\rho_g\,. \tag{44}$$

As in the inhalation case, the upper solution of equation (37) does not give representative values of pressure. The lower solution gives physically meaningful results. Note that the groups called "$\varepsilon_g\,, \zeta_g\,, \vartheta_g$ and κ_g", are equivalent to the groups "$\varepsilon\,, \zeta\,, \vartheta$ and κ" presented for the inhalation part of the process, but with the reference density ρ_0 substituted by the real gas density ρ_g.